Fluid Phase Equilibria 606 (2026) 114661

Contents lists available at ScienceDirect

Fluid Phase Equilibria

journal homepage: www.journals.elsevier.com/fluid-phase-equilibria

Thermodynamic modelling of dissociating Al_2Br_6 and Al_2Cl_6 used as reactive working fluids in thermodynamic cycles

Julien Joliat [a], Konstantin Samukov [a], Rachid Hadjadj [a], Thijs J.H. Vlugt [b], Olivier Herbinet [a], Silvia Lasala [a,*]

[a] Université de Lorraine, CNRS, LRGP, F-54000 Nancy, France
[b] Engineering Thermodynamics, Process & Energy Department, Faculty of Mechanical Engineering, Delft University of Technology, Leeghwaterstraat 39, Delft 2628CB, the Netherlands

ARTICLE INFO

Keywords:
Thermodynamic properties
Reactive working fluids
Equation of state
Monte Carlo, Simulations
Quantum chemistry calculations

ABSTRACT

To enhance the efficiency of thermodynamic cycles in heat pumps and power plants, we explore a novel approach: replacing conventional inert pure fluids or mixtures with reactive fluids that undergo reversible chemical reactions. A key step towards the implementation of this concept is the development of a fully predictive framework for determining the thermodynamic properties of such reactive working fluids. In this context, the present work extends a semi-empirical methodology previously proposed by the authors, aiming to address the challenge introduced by newly developed reactive fluids for which experimental data are unavailable. The methodology presented in this work requires only the critical-point properties and acentric factor of the molecules participating in the chemical reaction. As in the earlier approach from the authors, it combines ab-initio quantum mechanics calculations to determine the ideal gas properties of each molecule, the a-thermal version of the "Peng-Robinson + EoS/$a_{res}^{E,\gamma}$ mixing rules" equation of state and molecular Monte Carlo simulations to assess real fluid properties and enable cross-validation between methods. This work, however, applies a simplification to the force fields used in Monte Carlo simulations consisting in employing single-particle force fields instead of all-atom models. This strategy decreases the amount of experimental data required to parametrise the force field of each molecule contained in the reactive mixture, and allows the use of the same inputs in equation of state modelling and Monte Carlo simulations (i.e., molecular critical parameters). Indeed, this work proposes to calculate force field parameters using either the critical temperature and pressure, or the critical temperature and density of each molecule. The methodology is applied to two reactive systems, $Al_2Br_6 \rightleftharpoons 2AlBr_3$ and $Al_2Cl_6 \rightleftharpoons 2AlCl_3$. The results show that Monte Carlo predictions, although less accurate than those from the equation of state, remain acceptably close to experimental data, while the equation of state results demonstrate significantly higher accuracy.

1. Introduction

Thermodynamic cycles form the backbone of our current energy systems [1]. They are fundamental to the operation of thermal power plants – which still account for the majority of global electricity production – and heat pumps, whose installed capacity in the residential sector is expected to triple by 2030 and which are increasingly being deployed in the industrial sector [2]. Thermodynamic cycles are known today to operate with working fluids being chemically inert, all along the cycle [3,4]. With the aim to substantially increase the performance of power plants and heat pumps and to allow the more feasible use of heat pumps at industrial level, a quite unexplored approach investigated by the authors in the research projects REACHER [5] and CREATIVE [6], both funded by the European Research Council, proposes the use of working fluids being the site of a reversible chemical reaction. In particular, the considered chemical reactions consist of dimerization reactions, of the general form $A_2 \rightleftharpoons 2A$, which are able to proceed very rapidly towards chemical equilibrium states.

These reactions thus evolve across each unit operation as a consequence of the impact that the imposed changing of temperature and pressure has on the chemical equilibrium of the reaction. In preliminary studies using fictitious reactive fluids [7–9], Lasala et al. [7] have shown

* Corresponding author.
E-mail address: silvia.lasala@univ-lorraine.fr (S. Lasala).

https://doi.org/10.1016/j.fluid.2026.114661
Received 28 September 2025; Received in revised form 1 January 2026; Accepted 6 January 2026
Available online 8 January 2026

that the high-temperature dissociation of dimers into monomers and their reversible low-temperature association back into dimers throughout the cycle unit operations enable an increase in power cycle efficiency by nearly 30 % compared to chemically inert fluids. This effect was explained by Lasala et al. [8] as resulting from the compression of complex molecules (dimers) and the expansion of simple molecules (monomers), both enabled by the occurrence of a dimerization reaction. Barakat et al. [9] have theoretically demonstrated that the use of reactive instead of inert working fluids leads to a more than doubled coefficient of performance of the heat pump. Focusing on the latter contribution, the efficiency improvement was mainly attributed to the occurrence of an exothermic reaction in the hot heat exchanger (releasing more heat in the environment) and of an endothermic reaction in the compression process (requiring less energy to compress the fluid).

A review of previous studies on reactive working fluids, which is a concept dating back to the 1950s, is reported in previous publications from the authors [7,10,11]. In those works, the thermodynamic properties of three reactive fluids were characterised and their suitability for different applications was assessed: $N_2O_4 \rightleftharpoons 2NO_2$, $Al_2Br_6 \rightleftharpoons 2AlBr_3$, and $Al_2Cl_6 \rightleftharpoons 2AlCl_3$. Among these systems, dissociating N_2O_4 has been the most extensively studied, both from a thermodynamic and kinetic perspective. This is not the case for the systems $Al_2Br_6 \rightleftharpoons 2AlBr_3$, and $Al_2Cl_6 \rightleftharpoons 2AlCl_3$, for which kinetic data are currently unavailable. However, preliminary results from the analysis of the dimerisation reaction kinetics [8] suggest that the reaction rates are favourable for their potential use as working fluids in thermodynamic cycles.

Lasala et al. [10] recently proposed a generally applicable methodology to characterise the thermodynamic properties of dimerising reactive systems for which experimental data are available. This methodology was applied to the reactive system $N_2O_4 \rightleftharpoons 2NO_2$ and was based on Quantum Mechanics (QM) calculations, classical Monte Carlo (MC) simulations, and equation of state (EoS) modelling. Specifically, MC simulations performed by Lasala et al. [10] were based on available all-atom Lennard-Jones force fields. Also, the "Peng-Robinson + EoS/$a_{res}^{E,\gamma}$ mixing rules" equation of state [12] was used, which -in its a-thermal version- is a fully predictive model as it does not contain any adjustable binary interaction parameters to be optimised. Afterwards, Samukov et al. [11] proposed more accurate input properties (critical-point parameters and acentric factor of N_2O_4 and NO_2), with the same equation of state, enabling an improved modelling of dissociating N_2O_4. Specifically, these properties were optimised to improve the agreement between the model predictions and the experimental data.

Polat et al. [13] performed MC simulations of $N_2O_4 \rightleftharpoons 2NO_2$ and showed that the representation of N_2O_4 and NO_2 as single-particle Lennard-Jones force fields leads to accurate results, comparable with all-atom force fields used in the study of Lasala et al. [10]. However, the parameters of the single-particle Lennard-Jones force fields of N_2O_4 and NO_2 proposed by Polat et al. [13] were optimised on the MC results presented in Lasala et al. [10], for these two molecules.

Alternatively, single-particle Lennard-Jones force field parameters of N_2O_4 and NO_2 can be derived from their known critical properties, and these force fields can then be used to perform MC simulations on the reactive systems. This method is particularly suitable for modelling reactive systems for which experimental data available in the literature are insufficient to develop all-atom force fields, but whose critical points are available or can be estimated using predictive methods (e.g., by available machine learning models [14]). It is therefore highly useful for the characterization of new reactive fluids that have not yet been experimentally investigated. This is the main novel aspect introduced in the present work. Here, this approach is applied to characterise the $Al_2Br_6 \rightleftharpoons 2AlBr_3$ and $Al_2Cl_6 \rightleftharpoons 2AlCl_3$ systems, and further validated on $N_2O_4 \rightleftharpoons 2NO_2$.

The same EoS model, and the phase- and chemical-equilibrium algorithms employed in authors' previous works [10,11] are applied to predict the properties of $Al_2Br_6 \rightleftharpoons 2AlBr_3$ and $Al_2Cl_6 \rightleftharpoons 2AlCl_3$ systems. These predictions are then compared with MC simulation results. It is worth noting that both the selected EoS and MC simulations based on single-particle Lennard-Jones force fields require, as input, the ideal-gas properties obtained from Quantum Mechanics calculations, as well as the critical-point properties of the species forming the reactive mixture under investigation. This methodology is applied in a totally predictive way and enables the consistent comparison of computational tools (EoS and MC) requiring the same inputs.

In the following, Section 2 outlines the methodology used to compute thermochemical and thermophysical properties of the $Al_2Br_6 \rightleftharpoons 2AlBr_3$ and $Al_2Cl_6 \rightleftharpoons 2AlCl_3$ systems, while Section 3 presents the results, assesses their accuracy through comparison with available experimental data and concludes on the predictive capability of the methods applied in this study.

2. Methodology

In this work, MC molecular simulations were performed in conjunction with cubic equations of state to study the behaviour of two reactive fluid systems, $Al_2Br_6 \rightleftharpoons 2AlBr_3$ and $Al_2Cl_6 \rightleftharpoons 2AlCl_3$. The Monte Carlo method is founded on statistical mechanics and enables the calculation of macroscopic thermodynamic properties from molecular-level interactions [15,16]. Cubic equations of state are analytical thermodynamic models that approximate the macroscopic behaviour of fluids. The calculation of the thermodynamic properties of reactive fluids, both with MC simulations and an equation of state, requires the knowledge of the ideal gas properties of the molecules forming the reactive fluid. Section 2.1 details how ideal gas properties have been calculated in this work by QM calculations. Section 2.2 introduces the methodology applied to perform MC simulations. Section 2.3 presents the applied cubic equation of state and its considered parametrisation. A schematic of the proposed methodology is shown in Fig. 1.

2.1. Ideal gas properties calculation

QM calculations were performed to determine the thermochemical

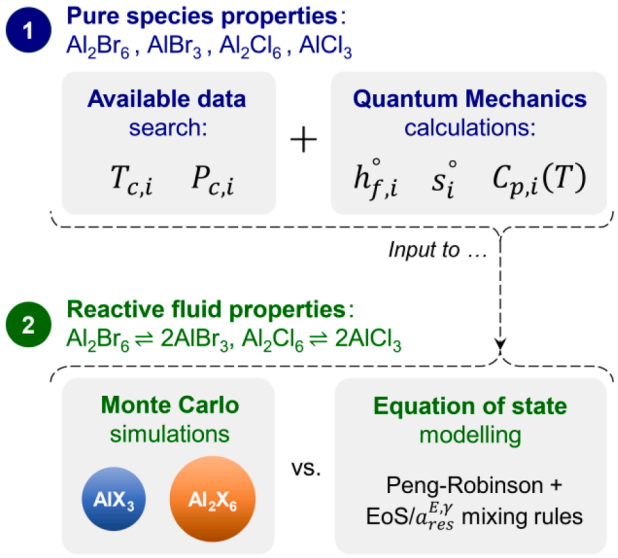

Fig. 1. Methodology applied in this work for predicting the vapour-liquid equilibrium properties of $Al_2Br_6 \rightleftharpoons 2AlBr_3$ and $Al_2Cl_6 \rightleftharpoons 2AlCl_3$. The workflow consists of: 1) searching available critical-point parameters of the pure species and computing their ideal gas properties by QM; and 2) using these data to determine and compare reactive fluid properties predicted via Monte Carlo simulations and equation of state modelling. AlX_3 denotes $AlCl_3$ or $AlBr_3$, Al_2X_6 denotes Al_2Cl_6 or Al_2Br_6.

properties of Al_2Cl_6, $AlCl_3$, Al_2Br_6, and $AlBr_3$. Geometry optimisation and frequency calculations were carried out using the Gaussian 09 software [17], employing the CBS-QB3 composite method [18], which is often used as it offers a compromise between computational cost and accuracy for simple molecules composed of atoms of the first three periods of the periodic table [19–22]. The literature shows that this method can also provide sufficient accurate data for species containing bromine atoms [23].

Specifically, the ideal-gas standard enthalpy of formation ($\Delta_f H^\circ$) at 298.15 K, the ideal-gas standard molar entropy (S°) at 298.15 K, and the ideal-gas heat capacities (C_p) were computed for Al_2Cl_6, $AlCl_3$, Al_2Br_6, and $AlBr_3$ between 298.15 K and 1500 K. These quantities have been derived from Gaussian's results as detailed below.

The standard enthalpies of formation at 298.15 K were evaluated using the atomisation method [24–27]:

$$\Delta_f H^\circ_{\mathrm{M}} = \left(H_{\mathrm{M,calc}} - \sum_i^N H_{i,\mathrm{calc}} \right) \cdot C + \sum_i^N \Delta_f H^\circ_{i,\mathrm{exp}} \tag{1}$$

Where M is the considered molecule, $H_{\mathrm{M,calc}}$ is the calculated ideal gas enthalpy of the fully optimised molecule, $H_{i,\mathrm{calc}}$ is the enthalpy of the i-th isolated atom forming the molecule, calculated at the same level of theory, N is the number of atoms of the molecule, C is a unit conversion factor (from Hartrees to kJ·mol^{-1}, equal to 2625.5 kJ·mol^{-1}·Hartrees^{-1}), and $\Delta_f H^\circ_{i,\mathrm{exp}}$ is the experimental standard enthalpy of formation of the i-th atom in the gas phase at 298.15 K. $\Delta_f H^\circ_{i,\mathrm{exp}}$ values have been taken from NIST database [28,29]. This approach ensures internal consistency in the thermochemical cycle and allows reliable evaluation of formation enthalpies from first principles.

Standard molar entropies, S°, were obtained firstly using:

$$S^\circ = \frac{H^\circ - G^\circ}{T} \tag{2}$$

Where H° and G° are the standard molar enthalpy and the Gibbs free energy of the molecule under consideration, calculated under ideal-gas conditions using Gaussian 09 [17], at a temperature T of 298.15 K. The standard molar entropies were then corrected by accounting for the molecular symmetry number, Ω, specific to each molecule:

$$S^\circ{}_{\mathrm{corr}} = S^\circ - R \cdot \ln(\Omega) \tag{3}$$

With R the ideal gas constant.

Additionally, temperature-dependant ideal gas heat capacities of each molecule $(C_p(T))$ were obtained from Gaussian's harmonic vibrational outputs using the Gaussian Post-Processing software (GPOP), developed by Miyoshi [30]. The computed $C_p(T)$ values have been fitted using the Aly-Lee equation [31], a commonly used empirical model for representing temperature-dependent thermodynamic properties. The Aly–Lee functional form is given by:

$$C_p(T) = A + B\left[\frac{\frac{C}{T}}{\sinh\left(\frac{C}{T}\right)}\right]^2 + D\left[\frac{\frac{E}{T}}{\cosh\left(\frac{E}{T}\right)}\right]^2 \tag{4}$$

With T the temperature in K and A, B, C, D, E adjustable parameters determined through regression. The fitting procedure was carried out by minimising the mean absolute percentage error (MAPE):

$$MAPE\% = \frac{100}{N}\sum_{i=1}^{N}\left|\frac{C_{p,\mathrm{GPOP}}(T_i) - C_{p,\mathrm{calc}}(T_i)}{C_{p,\mathrm{GPOP}}(T_i)}\right| \tag{5}$$

Where N is the number of temperature points, equal to 14 in this work, calculated with GPOP between 298.15 K and 1500 K, $C_{p,\mathrm{GPOP}}(T_i)$ is the heat capacity obtained from quantum chemical data and $C_{p,\mathrm{calc}}(T_i)$ is the heat capacity computed using Eq. (4). The same fitting procedure has been applied to determine $C_p(T)$-correlations for each molecule, on the basis of the values reported in JANAF tables [32]. The resulting A, B, C, D, E parameters of the correlation are reported in Section 3.1 (see Table 2 and Table 3 for the correlation based on the calculations of this work or on JANAF values, respectively).

2.2. Monte Carlo simulations

2.2.1. Lennard-Jones potential

To investigate the behaviour of reactive fluids by means of force field-based Monte Carlo simulations, it is necessary to define an intermolecular force field capable of representing dispersion and repulsion interactions between molecules, i.e., van der Waals interactions. The Lennard-Jones (LJ) potential was selected, as it is widely used in molecular simulations due to its simplicity and ability to capture the essential features of non-bonded interactions [33]. The functional form of the potential, U_{LJ}, is given as a function of the distance between the two molecules r, by:

$$U_{\mathrm{LJ}}(r) = 4\epsilon\left[\left(\frac{\sigma}{r}\right)^{12} - \left(\frac{\sigma}{r}\right)^{6}\right] \tag{6}$$

Where σ and ϵ are, respectively, the finite distance at which the potential energy is zero and the depth of the potential well, corresponding to the maximum strength of the attractive interaction. In this work, molecules Al_2Cl_6, $AlCl_3$, Al_2Br_6, and $AlBr_3$ have been modelled as single LJ particles, similarly to the approach of Polat et al. [13]. Consequently, Monte Carlo simulations of these reactive systems require only two parameters, σ and ϵ, for each molecule. It should be noted that representing both the dimeric halide (Al_2Cl_6 and Al_2Br_6) and monomer ($AlCl_3$ and $AlBr_3$) as isotropic single LJ spheres constitutes a strong coarse-graining, which neglects directional bonding, partial charges, and polarizability. However, this approach is intended to provide a physically consistent, first-order prediction of the vapour–liquid equilibrium (VLE) behaviour of reactive systems for which no detailed molecular data are available, rather than to capture fine anisotropic or electronic effects at the molecular scale. By deriving the LJ parameters (σ, ϵ) from experimentally measured -or reliably predicted- critical temperature, density, and pressure of the monomer and dimer, the model yields a physically grounded first-order description of their VLE properties, as demonstrated in Section 3.

Furthermore, although a less coarse-grained representation might suggest using dumbbell models for the dimers, such an approach would be less realistic, since their stable molecular configurations do not exhibit a distinct central Al–Al bond (see Figure S2 and Figure S4 of the Supplementary Material).

The calculation of σ and ϵ parameters of each molecule has been performed in this work using either Eqs. (7) and (8), or Eqs. (7) and (9). These expressions establish a correlation between the critical properties expressed in reduced units and the actual physical properties of the fluid components [16].

$$\epsilon = \frac{k_{\mathrm{B}} T_{\mathrm{c}}}{T^*_{\mathrm{c}}} \tag{7}$$

$$\sigma = \left(\frac{P^*_{\mathrm{c}}\epsilon}{P_{\mathrm{c}}}\right)^{1/3} \tag{8}$$

Where σ can also be determined by:

$$\sigma = \left(\frac{\rho^*_{\mathrm{c}}}{\rho_{\mathrm{c}}}\right)^{1/3} \tag{9}$$

Here, k_{B} is the Boltzmann constant, P_{c}, T_{c} and ρ_{c} denote the critical properties of the fluid. The uppercase "*" indicates that properties are expressed in reduced units and represent the critical properties of the LJ fluid [34], P^*_{c}, T^*_{c} and ρ^*_{c}. Given the critical parameters P_{c}, T_{c} and ρ_{c} from literature sources (listed for each molecule in Table 1), the calculation of σ and ϵ from either Eqs. (7) and (8), or Eqs. (7) and (9), requires only the corresponding reduced properties: T^*_{c} and P^*_{c}, or T^*_{c} and ρ^*_{c}. For

Table 1
Critical constants and acentric factor of dimeric and monomeric species [35].

Species	T_c (K)	P_c (bar)	V_c ($cm^3 \cdot mol^{-1}$)	ω (-)
Al_2Cl_6	625.7	26.34	528.1	0.296
$AlCl_3$	459.4	33.44	303.8	0.312
Al_2Br_6	768.0	27.05	601.3	0.350
$AlBr_3$	489.0	23.20	454.7	0.285

completeness (see Section 2.3), Table 1 also includes acentric factors. It should be noted that the procedure by which the data in Table 1 were obtained is not explicitly described. In particular, Ref. [35] does not provide details on how the properties of the monomer and the dimer were distinguished, although the reported dimerization reaction is known to occur on a very short timescale.

To ascertain the critical point of the Lennard-Jones fluid, preliminary simulations of a LJ fluid were carried out using the Gibbs Ensemble Monte Carlo (GEMC) method. In this work, the GEMC method is applied in its canonical form, corresponding to a GEMC–NVT ensemble, where the total number of molecules, the total simulation volume, and the temperature are conserved, while particle exchanges between boxes and volume redistributions are permitted [36,37]. Simulations were conducted using the Brick-CFCMC simulation code [38–40], which was consistently used throughout the present work for all Monte Carlo calculations. Brick-CFCMC uses the Continuous Fractional Component Monte Carlo (CFCMC) technique to facilitate molecule transfers between simulation boxes. In this technique, a so-called fractional molecule has scaled interactions with surrounding molecules governed by a parameter λ, such that $\lambda = 0$ corresponds to a fractional molecule with no interactions with the surrounding molecules, and $\lambda = 1$ corresponds to full interactions. Trial moves to sample values of λ (λ-moves) are included in the simulation. For additional methodological details, the reader is referred to Refs. [38–40]. Each GEMC simulation was performed in a two-box configuration, representing the coexisting liquid and vapour phases, and was repeated five times with independent initial configurations to ensure statistical reproducibility and reliable uncertainty quantification. In each simulation, 750 molecules were used in total. Initially, 600 molecules were placed in the first cubic box and 150 molecules in the second, with both boxes having a box length of 13.339 σ [41]. The intermolecular interactions were modelled using the Lennard-Jones potential, with a cut-off radius set to 2.5 σ. Long-range tail corrections were included to compensate for the contributions beyond the cut-off distance. The set of Monte Carlo moves was composed of translational displacements (49 %), volume exchange moves (1 %), identity swap and molecule exchange moves (30 %), and λ-moves (20 %), enabling efficient sampling of the phase space. Each simulation consisted of $3 \cdot 10^5$ equilibration Monte Carlo cycles, followed by 10^6 production cycles for statistical averaging and data collection. Each cycle consisted of 750 trial moves. In the case of the LJ fluid, the saturation pressure was calculated by conducting isothermal–isobaric (NPT) simulations in parallel with GEMC simulations, to map the gas phase coexistence density observed in GEMC to those predicted by NPT calculations. These NPT simulations were conducted with 500 molecules in a cubic box with an initial side length of 100 σ. After 10^5 equilibration cycles, $2 \cdot 10^5$ production cycles were performed, each consisting of 500 trial moves. The attempted moves were distributed as 95 % translational displacements and 5 % volume changes. The same cut-off radius of 2.5 σ was used, and long-range tail corrections were included for energy. For each NPT and GEMC simulation, independent random seeds were used to ensure statistical independence, and block averaging over 10^3 cycles was performed during the production stage to evaluate statistical uncertainties. The critical parameters were obtained in this work from the numerical fitting of the scaling laws, Eqs. (10)-(12), to the simulation data.

$$\rho_l^* - \rho_g^* = A\left(T^* - T_c^*\right)^\beta \tag{10}$$

$$\frac{\rho_l^* + \rho_g^*}{2} = \rho_c^* + B\left(T^* - T_c^*\right) \tag{11}$$

$$\ln P^{sat,*} = C + \frac{D}{T^*} \tag{12}$$

It is highlighted that Eqs. (10)-(12) are commonly used in molecular simulations of phase equilibria to characterise critical behaviour [15,42]. In Eqs. (10)-(12), all the physical quantities are expressed in reduced units [15,16] to obtain universal results for the LJ fluid. In Eq. (10), the critical exponent, $\beta = 0.32$, reflects the universal scaling behaviour near the critical point for simple fluids. Eqs. (10) and (11) allow the extrapolation of T_c^* and ρ_c^* from the coexistence densities ρ_l^* and ρ_g^*, densities of the liquid and gas phase, respectively. Eq. (12) expresses the saturation pressure, $P^{sat,*}$, as a function of temperature T^*; in this work, the determination of Eq. (12), i.e. of C and D, enables the estimation of the critical pressure from the knowledge of the critical temperature, previously determined from Eqs. (10) and (11). Other simulation parameters were maintained at the default settings of Brick-CFCMC [38,40].

2.2.2. Monte Carlo simulations in the reactive Gibbs ensemble

To model chemical reactions at VLE conditions, simulations were performed using the reaction ensemble Monte Carlo method (RxMC) [43–45], combined with the Gibbs ensemble. This hybrid RxMC/GEMC framework is referred to as the Reactive Gibbs Ensemble (RGE) throughout this work. The Continuous Fractional Component (CFC) approach was used to facilitate chemical transformations and improve sampling efficiency [46]. Specifically, the simulations were conducted using two distinct simulation boxes, representing the coexisting vapour and liquid phases. The total volume, V, of the system was maintained constant, while volume exchange moves between the boxes were allowed to ensure thermodynamic equilibrium [10,13,47]. Unless otherwise specified, default Brick-CFCMC settings were used for all other simulation details [38,40].

This approach relies on trial Monte Carlo moves in which reactant molecules are deleted from the simulation box, while reaction product molecules are inserted, and vice versa, in a manner that satisfies detailed balance and allows the system to reach chemical equilibrium. In this method, equilibrium is sampled by Monte Carlo moves, without consideration of kinetics or reaction mechanisms. The acceptance criteria for trial moves depend on the chemical reaction equilibrium constant, which in turn requires the ideal-gas partition functions of all species involved (reactants and products) [38]. These partition functions were obtained from QM calculations using the CBS-QB3 composite method [18]. Further details on the calculated quantum mechanical input required for the RGE simulations can be found in Table S7 of the Supplementary Material.

For binary systems involving both monomers (A) and dimers (A_2), the initial number of molecules was set to 500, with 400 molecules (A_2) placed in the first cubic simulation box and 100 molecules (A) in the second. These numbers were allowed to fluctuate throughout the simulation due to reaction moves and phase exchanges. The initial volume of the system was estimated using Eq. (13):

$$V = \frac{N M_w}{N_a \frac{\rho}{2}} \tag{13}$$

where N is the number of molecules, M_w the molecular weight, N_a Avogadro's number, and ρ the estimated density.

The initial edge lengths of the cubic simulation boxes were then set to 69.577 Å for the $Al_2Cl_6 \leftrightharpoons 2AlCl_3$ system and 75.802 Å for the $Al_2Br_6 \leftrightharpoons 2AlBr_3$ system. Interactions were modelled using the specific Lennard-Jones potential with a cut-off distance of 2.5 σ_{max}, where σ_{max} is

the largest Lennard-Jones diameter obtained from the Lorentz-Berthelot combining rules [15]. This choice resulted in cut-off distances of 16.1775 Å and 16.8025 Å for the $Al_2Cl_6 \rightleftharpoons 2AlCl_3$ system, and of 16.8925 Å and 17.8300 Å for the $Al_2Br_6 \rightleftharpoons 2AlBr_3$ system, depending on the selected initial parameters (see Section 3.2.1). Long-range tail corrections were applied to account for interactions beyond the cut-off. The Monte Carlo move set was composed of translational displacements (39 %), volume change moves (1 %), identity swap and molecule exchange moves (20 %), λ-moves (20 %), and reaction moves (20 %). Each RGE simulation was initialized with an independent random seed to ensure statistical independence. The simulations are based on $3{\cdot}10^5$ equilibration cycles, followed by $3{\cdot}10^6$ production cycles, during which pressure was calculated from the virial equation [15]. Statistical uncertainties were quantified by block averaging over 10^4 cycles during the production stage.

2.3. Equation of state modelling

Similarly to the modelling choice made in our previous works focussing on the thermodynamic representation of $N_2O_4 \rightleftharpoons 2NO_2$ [10, 11], the equation of state used in this study to model the properties of the considered reactive fluid mixtures is the cubic Peng–Robinson equation of state [48], Eq. (14), coupled with advanced EoS/$a_{res}^{E,\gamma}$ mixing rules [12], Eq. (15):

$$P = \frac{RT}{V - b_m} - \frac{a_m}{V(V + b_m) + b_m(V - b_m)} \tag{14}$$

$$\begin{cases} b_m = \sum_i z_i b_i \\ \dfrac{a_m}{b_m} = \sum_i z_i \dfrac{a_i}{b_i} + \dfrac{a_{res}^{E,\gamma}}{\Lambda_{EoS}} \end{cases} \tag{15}$$

Where V is the molar volume, R is the ideal gas constant, $a_{res}^{E,\gamma}$ is the residual Helmholtz energy term calculated from an activity coefficient (γ) model, Λ_{EoS} is a numerical parameter being a function of the considered equation of state, a_m and b_m are the energy and co-volume parameters of the reactive mixture, a_i and b_i are the energy and co-volume parameters of the molecules forming the mixtures, and are calculated from Eqs. (16) and (17) as a function of the critical temperature, critical pressure and acentric factor.

$$b_i = 0.0778 \frac{RT_{c,i}}{P_{c,i}} \tag{16}$$

$$a_i(T) = 0.45724 \frac{(RT_{c,i})^2}{P_{c,i}} \left(1 + m_i\left(1 - T_{r,i}^{0.5}\right)\right)^2 \tag{17}$$

where m_i is a function of the acentric factor (ω_i), and $T_{r,i}$ is the reduced temperature of the considered species.

Moreover, this work applies a zero-residual excess Helmholtz energy term, $a_{res}^{E,\gamma} = 0$: the reactive mixtures are treated as a-thermal systems because the intermolecular forces between the considered dimeric molecules are weak, as for the interactions between dimers and monomers. In contrast, the interaction between radicals (monomers) is strong and drives the association reaction, which is explicitly accounted for as a chemical reaction in the model. By assuming zero residual excess Helmholtz energy, the model avoids the introduction of semi-empirical binary interaction parameters (otherwise required in residual excess Helmholtz formulations) and can therefore be used in a fully predictive manner.

The critical temperature, pressure and acentric factor used in this study are reported in Table 1. A detailed justification for the choice of the model can be found in Lasala et al. [10]. The energetic properties of the reactive mixture - namely, enthalpy h and entropy s - were determined by combining the ideal-gas contributions of each molecule ($\Delta_f H^\circ$, S°, $C_p(T)$) with the residual contributions derived from the equation of state, in accordance with the methodology outlined by Elliot and Lira [49].

Before concluding this methodological section, it is important to observe that if single-site LJ potential parameters of Al_2Br_6, $AlBr_3$, Al_2Cl_6, and $AlCl_3$ are derived from T_c and P_c, instead of T_c and V_c, EoS modelling and MC simulations are consistently applied on the basis of a common set of inputs: T_c and P_c of those molecules, available in the literature or obtained from reliable predictive methods, and their ideal gas properties, determined in this work by quantum mechanics ab-initio calculations. The selected EoS modelling requires also the knowledge of the acentric factor of each molecule.

3. Results

3.1. Ideal gas properties

The thermodynamic properties obtained from QM calculations are shown in Table 2. For comparison, Table 3 collects the properties available in JANAF tables. A good agreement is obtained for entropy (relative uncertainties below 1 %). Higher deviations are observed for the enthalpy of formation of chlorinated species (relative uncertainties of 6 %, in agreement with the CBS-QB3 method benchmark [19]) and of brominated species (relative uncertainties up to 17 %). These deviations could be resolved by considering empirical corrections in the atomization method (bond additivity and spin-orbit corrections) [22], but they are unfortunately not available for the systems studied in the present work due to the lack of experimental data. The calculated optimised geometries are presented in the Supplementary Material (Figures S1-S4 and Tables S1-S4).

The determined standard enthalpies of formation ($\Delta_f H^\circ$) and standard entropies (S°) of monomers and dimers allow the calculation of the standard enthalpy and entropy of reaction, $\Delta_R H^\circ_{298.15\ K}$ and $\Delta_R S^\circ_{298.15\ K}$, respectively (see Table 4). Taking into account experimental uncertainties, the comparison between calculated and available standard enthalpies of formation ($\Delta_f H^\circ$), standard entropies (S°) and reaction values shows a very good agreement for the system $Al_2Cl_6 \rightleftharpoons 2AlCl_3$, and satisfactory accuracy for $Al_2Br_6 \rightleftharpoons 2AlBr_3$. These results support the reliability of thermochemical data obtained from ab-initio calculations, validating their use as input for the proposed predictive methodology aimed at the preliminary thermodynamic characterization of dimerization reactions.

As previously noted by Samukov et al. [11], even small uncertainties in ideal gas properties can have a significant influence on the calculation of thermodynamic properties at vapour-liquid equilibrium. This observation is further reinforced in the present work, as discussed in Section 3.2.2. Accordingly, in the following thermodynamic calculations, the widely accepted JANAF ideal gas values have been used, rather than ab-initio results obtained in this study.

3.2. Real fluid properties

3.2.1. Lennard-Jones fluid

GEMC simulations were performed for the Lennard-Jones (LJ) fluid using the Brick-CFCMC simulation package. The resulting coexistence densities are shown in Fig. 2(a), where the temperature is plotted as a function of liquid and vapour densities. In parallel, NPT simulations were conducted under the same thermodynamic conditions to compute the corresponding saturation pressures. This approach enabled the mapping of GEMC-derived densities onto NPT-determined pressures. The pressure–temperature data points are presented in Fig. 2(b).

The LJ-fluid critical parameters have been obtained from MC results shown in Fig. 2 and Eqs. (10)-(12), as described in Section 2.2.1:

$$T_c^* = 1.302 \pm 0.001, \quad \rho_c^* = 0.309 \pm 0.001, \quad P_c^* = 0.121 \pm 0.001 \tag{18}$$

Table 2
Parameters of the $C_p(T)$-correlation in Eq. (4) determined from QC data obtained in this work as described in Section 2.1, and thermochemical data from this work.

Species	A ($J \cdot mol^{-1} \cdot K^{-1}$)	B ($J \cdot mol^{-1} \cdot K^{-1}$)	C (K)	D ($J \cdot mol^{-1} \cdot K^{-1}$)	E (K)	$\Delta_f H^\circ_{298.15\ K}$ ($J \cdot mol^{-1}$)	$S^\circ_{298.15\ K}$ ($J \cdot mol^{-1} \cdot K^{-1}$)
Al_2Cl_6	89.73132	93.18688	416.1516	65.5322	209.905	–1,376,512	470.439
$AlCl_3$	53.04456	30.10001	667.3003	27.8962	336.756	–620,380	314.314
Al_2Br_6	83.42980	99.48834	296.6658	75.7347	138.357	–1,075,422	543.459
$AlBr_3$	56.74903	26.39557	563.6125	24.8108	283.920	–479,222	349.142

Table 3
Parameters of the $C_p(T)$-correlation in Eq. (4) determined from JANAF data [32] as described in Section 2.1, and thermochemical data from JANAF [32].

Species	A ($J \cdot mol^{-1} \cdot K^{-1}$)	B ($J \cdot mol^{-1} \cdot K^{-1}$)	C (K)	D ($J \cdot mol^{-1} \cdot K^{-1}$)	E (K)	$\Delta_f H^\circ_{298.15\ K}$ ($J \cdot mol^{-1}$)	$S^\circ_{298.15\ K}$ ($J \cdot mol^{-1} \cdot K^{-1}$)
Al_2Cl_6	75.54475	107.37209	390.1408	75.8802	188.447	–1,295,743 ± 3,350	475.050 ± 4.2
$AlCl_3$	42.46679	40.67717	409.0577	25.1172	188.797	–584,588 ± 2,900	314.494 ± 2.9
Al_2Br_6	91.59179	91.32532	321.8625	61.9995	156.460	–937,216 ± 3,400	547.220 ± 4.2
$AlBr_3$	46.51004	36.63410	345.3512	23.4256	157.507	–410,450 ± 1,700	349.441 ± 1.26

Table 4
Standard enthalpies and entropies of reaction, $\Delta_R H^\circ_{298.15\ K}$ and $\Delta_R S^\circ_{298.15\ K}$, for the considered systems.

Reaction	$\Delta_R H^\circ_{298.15\ K,\ JANAF}$ ($kJ \cdot mol^{-1}$)	$\Delta_R S^\circ_{298.15\ K\ JANAF}$ ($J \cdot mol^{-1} \cdot K^{-1}$)	$\Delta_R H^\circ_{298.15\ K,\ this\ work}$ ($kJ \cdot mol^{-1}$)	$\Delta_R S^\circ_{298.15\ K\ this\ work}$ ($J \cdot mol^{-1} \cdot K^{-1}$)
$Al_2Cl_6 \rightleftharpoons 2AlCl_3$	126.567	153.938	135.752	158.189
$Al_2Br_6 \rightleftharpoons 2AlBr_3$	116.316	151.662	116.978	154.825

These values are very similar to those reported in the literature for the Lennard-Jones fluid [34]. The values of parameters A-D, fitted with LJ-fluid critical parameters as described in Section 2.2.1, are reported in the Supplementary Material (Table S8).

The Lennard-Jones parameters ϵ and σ determined from the critical coordinates available in the literature (see Table 1), and used to perform MC simulations of the $Al_2Cl_6 \leftrightharpoons 2AlCl_3$ and $Al_2Br_6 \leftrightharpoons 2AlBr_3$ reactions, are reported in Table 5. According to Eqs. (8) and (9), the σ parameter may take two possible values depending on whether it is derived from P_c or from V_c, where the critical specific volume V_c corresponds to the inverse of the critical density ρ_c. In Section 3.2.2, the impact of using σ calculated from either T_c and V_c, or T_c and P_c, is quantified and discussed.

3.2.2. Monte Carlo simulations of reactive fluids and modelling by an equation of state

The VLE properties of the reactive mixtures are computed using two parallel approaches: reactive Gibbs ensemble MC (RGE) simulations and thermodynamic predictions based on an advanced cubic equation of

Table 5
Lennard-Jones parameter values calculated in this work and used for MC simulations.

Species	ϵ/k_B(K)	σ (Å)	
		(T_c, V_c)	(T_c, P_c)
Al_2Cl_6	480.568	6.471	6.721
$AlCl_3$	352.842	5.382	5.599
Al_2Br_6	589.862	6.757	7.132
$AlBr_3$	375.576	6.156	6.458

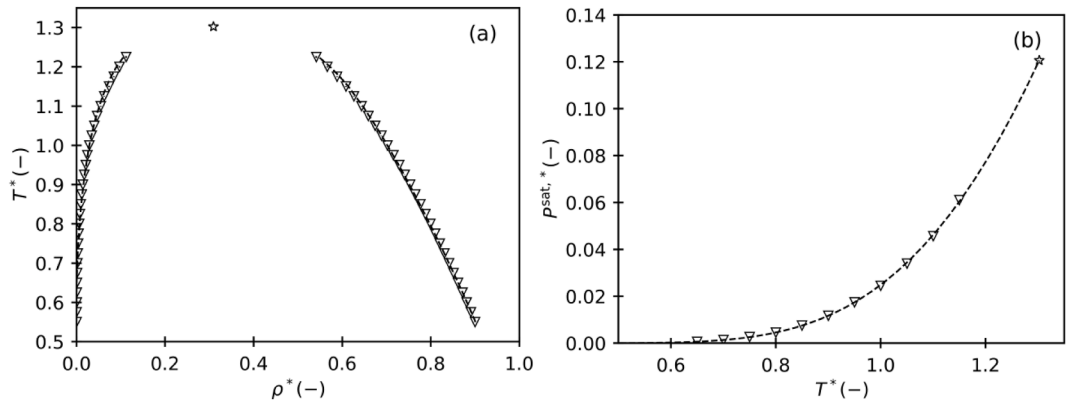

Fig. 2. Lennard-Jones fluid phase diagrams. (a) Coexistence density profile. (b) Saturation pressure as a function of temperature. In both figures: Black downward triangles represent the results obtained from RGE simulations; the black star represents the calculated critical point (see Eq. (18)); the black dashed curves correspond to the fitted correlation based on Eq. (10) – figure (a) – and Eq. (12) – figure (b). Error bars are included for the MC simulation results; however, they are smaller than the symbol size and may therefore not be visually distinguishable.

state, as discussed in Sections 2.2 and 2.3, respectively. It is highlighted that, for these two approaches, the only external inputs are the critical parameters and acentric factors of Al_2Br_6, $AlBr_3$, Al_2Cl_6 and $AlCl_3$. In this section, the results are shown and compared with experimental data available in the literature, in order to assess the accuracy and predictive capability of the two simulation methods. The numerical values of MC simulation results are reported in Section S4 of the Supplementary Material.

The VLE densities and pressures obtained from Monte Carlo simulations, along with experimental values reported in the literature, are presented in Fig. 3 and Fig. 4, respectively. Fig. 3(a) and Fig. 4(a) show the results for the reactive mixture $Al_2Br_6 \leftrightharpoons 2AlBr_3$, while Fig. 3(b) and Fig. 4(b) present data of the system $Al_2Cl_6 \leftrightharpoons 2AlCl_3$. The comparison between these two systems shows that the temperature–density (T-ρ) diagram of $Al_2Cl_6 \leftrightharpoons 2AlCl_3$ exhibits a critical region occurring at lower densities compared to the $Al_2Br_6 \leftrightharpoons 2AlBr_3$ system. This behaviour reflects the smaller molecular size and weaker van der Waals interactions of the chloride-based species, resulting in a lower critical density and temperature. In both cases, the VLE volumetric behaviour calculated by MC simulations for the two chemical systems captures the experimental datasets with a qualitatively sufficient first-order accuracy level. However, the accuracy of calculated VLE pressures is affected by important deviations with respect to experimental values.

Fig. 3 and Fig. 4 also show that the use of a different set of (σ, ϵ)-parameters calculated either from (T_c, P_c) or (T_c, V_c) has a non-negligible impact on the VLE properties: the best representation of VLE densities (Fig. 3) and pressures (Fig. 4) is guaranteed by the use of (σ, ϵ)-parameters calculated from (T_c, V_c) and (T_c, P_c), respectively. Hence, each parametrisation consistently reproduces at best the property from which it is derived.

A quantitative analysis of MC accuracy is presented below, with reference to EoS results. The deviation of the equation of state from experimental data is also assessed.

Fig. 5 and Fig. 6 compare the results of the equation of state (Section 2.3) with available experimental data, and MC simulation results determined with the use of input (σ, ϵ)-parameters calculated, for simplicity, only from (T_c, V_c). It is recalled that the results obtained from the use of (T_c, P_c) are reported in Fig. 3 and Fig. 4.

The overall methodology exhibits a satisfactory first-order predictive performance (see Table 6 and Table 7):

- **Liquid density at vapour-liquid equilibrium conditions**. Using (σ, ϵ)-parameters derived from (T_c, V_c), the mean absolute percentage error (MAPE) and average absolute deviation (AAD) between MC simulations and EoS modelling are 3.4 % and 70.2 kg·m^{-3} for $Al_2Br_6 \leftrightharpoons 2AlBr_3$, 7.3 % and 93 kg·m^{-3} for $Al_2Cl_6 \leftrightharpoons 2AlCl_3$. When ($T_c, P_c$) is used as input, the deviations increase substantially. Comparisons between EoS and experimental data yield MAPE and AAD values of 4.5 % and 69.7 kg·m^{-3} for $Al_2Br_6 \leftrightharpoons 2AlBr_3$, 3.8 % and 36.6 kg·m^{-3} for $Al_2Cl_6 \leftrightharpoons 2AlCl_3$.
- **Vapour density at vapour-liquid equilibrium conditions**. For (σ, ϵ)-parameters obtained from (T_c, V_c), the MAPE and AAD between MC simulations and EoS modelling are 114.6 % and 52.6 kg·m^{-3} for $Al_2Br_6 \leftrightharpoons 2AlBr_3$, 128.4 % and 21.5 kg·m^{-3} for $Al_2Cl_6 \leftrightharpoons 2AlCl_3$. The MAPE and AAD between experimental data and EoS predictions are 13.3 % and 33.7 kg·m^{-3} for $Al_2Br_6 \leftrightharpoons 2AlBr_3$, and 6.8 % and 5.3 kg·m^{-3} for $Al_2Cl_6 \leftrightharpoons 2AlCl_3$.
- **Pressure at vapour-liquid equilibrium conditions**. EoS predictions show significantly better agreement than RGE simulations: with AAD of 0.1–0.2 bar versus 2.7 - 4.9 bar; and MAPE of 3.2–5 % versus 91.7 %−153.8 %.

For completeness, Fig. 7 presents the unique non-isothermal ($P-\{x_1, y_1\}$) phase diagram [10] of both $Al_2Br_6 \leftrightharpoons 2AlBr_3$ (Figure 7 (a)) and $Al_2Cl_6 \leftrightharpoons 2AlCl_3$ (Figure 7(b)), where x is the molar composition of the liquid phase and y is the one of the vapour phase, and where component "1 is the monomer. Quantitative deviations among EoS and MC results are reported in Table 6 and Table 7. Fig. 7 indicates that the amount of monomer in both reactive fluids is very low at VLE conditions, particularly for the system $Al_2Cl_6 \leftrightharpoons 2AlCl_3$. The chemical reaction exhibits only a minor influence in this system, both in the saturated liquid phase and in the vapour phase. This is not the case for the system $Al_2Br_6 \leftrightharpoons 2AlBr_3$. Considering the order of magnitude of molar fractions, it can be observed that the equation of state reproduces the trend of MC simulation data with an acceptable accuracy level. Also, the phase diagrams of $Al_2Br_6 \leftrightharpoons 2AlBr_3$ in Figure 7(a) show that the main cause of the observed deviations between RGE and EoS calculations is related to the difference in the calculation of the pure dimer saturation pressure, at $\{x_1 = 0, y_1 = 0\}$. This is due to the inaccuracy in the calculation of saturation pressures by MC, as already mentioned above and quantified in Table 6 and Table 7.

For the considered systems, the chemical reaction becomes more pronounced at higher temperatures, in the gas phase. This can be observed in the temperature-entropy diagrams in Fig. 8, calculated with the equation of state presented in Section 2.3, where subcritical isobars exhibit inflection points that characterise the occurrence of chemical

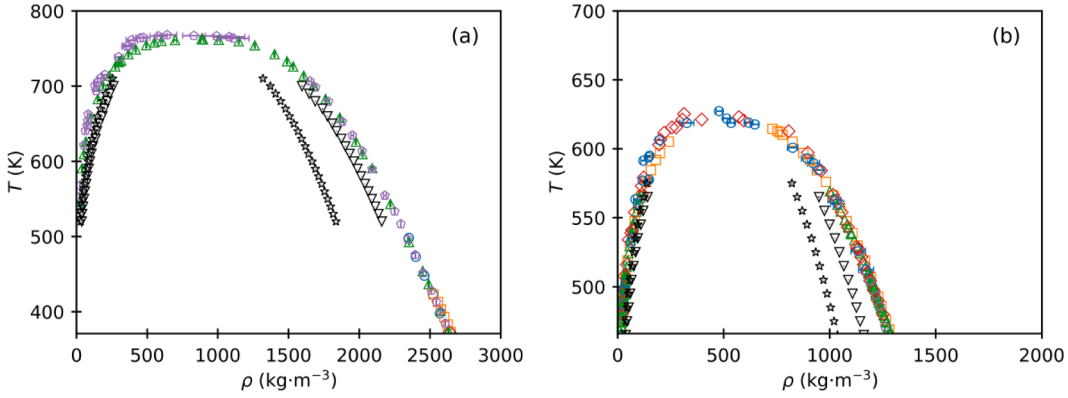

Fig. 3. Coexistence densities of the reactive mixture: (a) $Al_2Br_6 \leftrightharpoons 2AlBr_3$ and (b) $Al_2Cl_6 \leftrightharpoons 2AlCl_3$. In both figures: black downward triangles represent RGE simulation results using $(T_c, V_c) - (\sigma, \epsilon)$-parameter set, black stars represent RGE simulation results using $(T_c, P_c) - (\sigma, \epsilon)$-set. Moreover, (a) Blue circles correspond to experimental data from Biltz and Voigt [50]; orange squares to Gorenbejn [51]; red diamonds to Kločko [52]; green upward triangles to Johnson et al. [53]; and purple pentagons to Nisel'son et al. [54]. (b) Blue circles correspond to data from Denisova and Baskova [55]; orange squares to Johnson et al. [56]; red diamonds to Nisel'son and Sokolova [57]; green upward triangles to King and Seemiller [58]; and purple pentagons to Sato et al. [59]. Error bars are indicated in the figure whenever they were reported in the respective references. Error bars are included for the RGE simulation results; however, they are smaller than the symbol size and may therefore not be visually distinguishable.

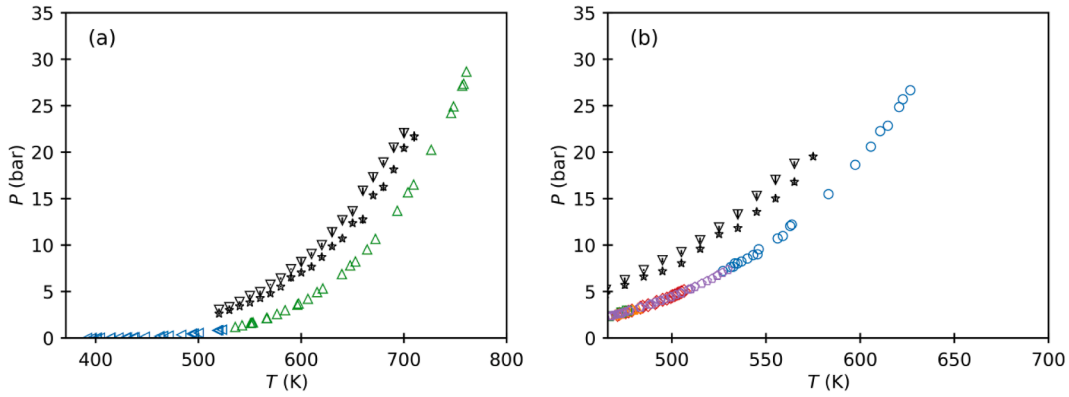

Fig. 4. Pressure of the reactive systems at vapour-liquid equilibrium condition: (a) $Al_2Br_6 \rightleftharpoons 2AlBr_3$ and (b) $Al_2Cl_6 \rightleftharpoons 2AlCl_3$. In both figures, black downward triangles represent RGE simulation results using $(T_c, V_c) - (\sigma, \epsilon)$-parameter set, black stars represent RGE simulation results using $(T_c, P_c) - (\sigma, \epsilon)$-set. (a) Blue left triangles correspond to data from Fischer et al. [60], green triangles to Johnson et al. [61]. (b) Black downward triangles represent RGE simulation results; blue circles correspond to data from Denisova and Baskova [55]; red diamonds to Nisel'son et al. [62]; orange triangles to Smits et al. [63–65]; green squares to Treadwell and Terebesi [66]; and purple pentagons to Viola et al. [67]. Error bars are indicated in the figure whenever they were reported in the respective references. Error bars are included for the RGE simulation results; however, they are smaller than the symbol size and may therefore not be visually distinguishable.

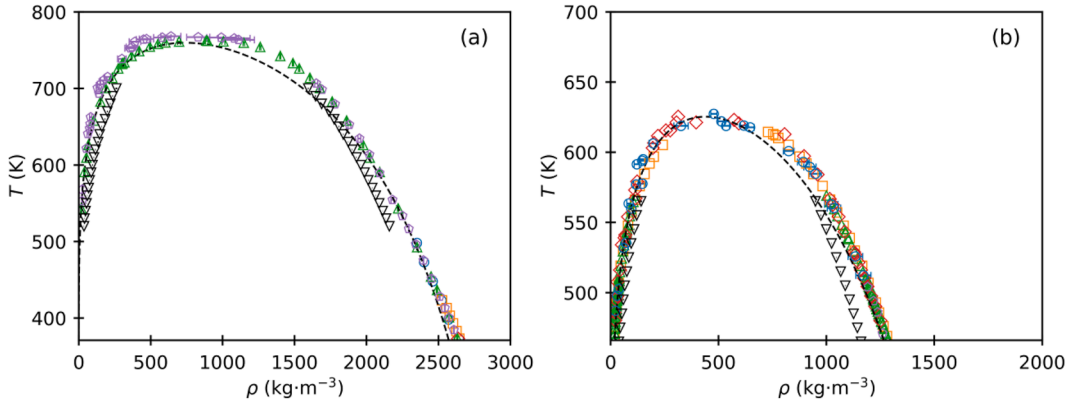

Fig. 5. $T - \rho$ diagram of the reactive mixture: (a) $Al_2Br_6 \rightleftharpoons 2AlBr_3$ and (b) $Al_2Cl_6 \rightleftharpoons 2AlCl_3$. In both figures: black downward triangles represent RGE simulation results using $(T_c, V_c) - (\sigma, \epsilon)$-parameter set. Moreover, (a) Blue circles correspond to experimental data from Biltz and Voigt [50]; orange squares to Gorenbejn [51]; red diamonds to Kločko [52]; green upward triangles to Johnson et al. [53]; and purple pentagons to Nisel'son et al. [54]. (b) Blue circles correspond to data from Denisova and Baskova [55]; orange squares to Johnson et al. [56]; red diamonds to Nisel'son and Sokolova [57]; green upward triangles to King and Seemiller [58]; and purple pentagons to Sato et al. [59]. Error bars are indicated in the figure whenever they were reported in the respective references. Error bars are included for the RGE simulation results; however, they are smaller than the symbol size and may therefore not be visually distinguishable. Black dotted line represents the result of the equation of state modelling, obtained using JANAF thermochemical data (Table 3).

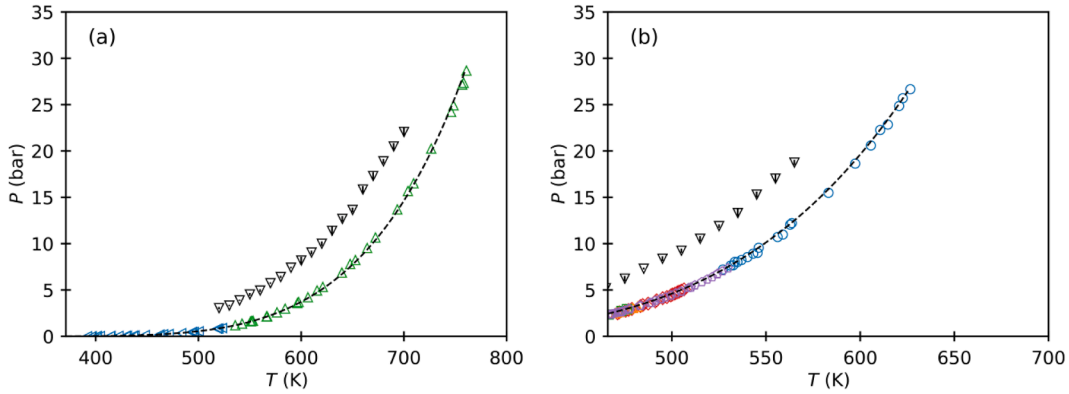

Fig. 6. Pressure of the reactive systems at vapour-liquid equilibrium condition: (a) $Al_2Br_6 \rightleftharpoons 2AlBr_3$ and (b) $Al_2Cl_6 \rightleftharpoons 2AlCl_3$. In both figures, black downward triangles represent RGE simulation results using $(T_c, V_c) - (\sigma, \epsilon)$-parameter set. (a) Blue left triangles correspond to data from Fischer et al. [60], green triangles to Johnson et al. [61]. (b) Blue circles correspond to data from Denisova and Baskova [55]; red diamonds to Nisel'son et al. [62]; orange triangles to Smits et al. [63–65]; green squares to Treadwell and Terebesi [66]; and purple pentagons to Viola et al. [67]. Error bars are indicated in the figure whenever they were reported in the respective references. Error bars are included for the RGE simulation results; however, they are smaller than the symbol size and may therefore not be visually distinguishable. Black dotted line represents the result of the equation of state modelling, obtained using JANAF thermochemical data (Table 3).

Table 6
Mean Absolute Percentage Error (MAPE) between Monte Carlo simulation results, Equation of State calculations and experimental data; to enable a comparison, the common reference in these relative deviations is the EoS value. "X" is either Br or Cl atom. "n.a." means "not available".

Systems and compared data		MAPE (%)				
		ρ_l	ρ_v	P^{VLE}	x AlX_3	y AlX_3
$Al_2Br_6 \leftrightharpoons 2AlBr_3$	Experimental vs. EoS data	**4.5**	**13.3**	**5**	n.a. exp. values	n.a. exp. values
	MC (T_c,V_c) vs. EoS data	3.4	114.6	124.5	45.9	50.9
	MC (T_c,P_c) vs. EoS data	17.1	79.7	91.7	27.5	41.8
$Al_2Cl_6 \leftrightharpoons 2AlCl_3$	Experimental vs. EoS data	**3.8**	**6.8**	**3.2**	n.a. exp. values	n.a. exp. values
	MC (T_c,V_c) vs. EoS data	7.3	128.4	153.8	99	99.1
	MC (T_c,P_c) vs. EoS data	16.9	99	124.6	98.3	98.6

Table 7
Average Absolute Deviation (AAD) between Monte Carlo simulation results, Equation of State calculations and experimental data; to enable a comparison, the common reference in these relative deviations is the EoS value. "X" is either Br or Cl atom. "n.a." means "not available".

Systems and compared data		AAD				
		ρ_l ($kg{\cdot}m^{-3}$)	ρ_v ($kg{\cdot}m^{-3}$)	P^{VLE} (bar)	x AlX_3 (-)	y AlX_3 (-)
$Al_2Br_6 \leftrightharpoons 2AlBr_3$	Experimental vs. EoS data	69.7	33.7	0.1	n.a. exp. values	n.a. exp. values
	MC (T_c,V_c) vs. EoS data	70.2	52.6	4.9	0.004	0.02
	MC (T_c,P_c) vs. EoS data	339.8	35.3	3.6	0.002	0.02
$Al_2Cl_6 \leftrightharpoons 2AlCl_3$	Experimental vs. EoS data	36.6	5.3	0.2	n.a. exp. values	n.a. exp. values
	MC (T_c,V_c) vs. EoS data	93.0	21.5	3.4	0.0004	0.002
	MC (T_c,P_c) vs. EoS data	210.1	15.7	2.7	0.0003	0.001

reactions, whereas the inflection observed on supercritical isobars arises from the proximity to the critical point. The saturation curve of these diagrams shows that the two fluids are *dry* fluids, meaning that the slope of the saturated vapour locus guarantees a superheated fluid's expansion in the turbine of a saturated Rankine cycle [68]. Moreover, in the considered temperature and pressure intervals, the two reactions evolve almost completely, confirming the possibility of exploiting the already proven positive reaction features [7–9] in thermodynamic cycles operating with reactive working fluids.

3.2.3. Critical point properties

The critical temperature, pressure, and density of the two reactive systems, $Al_2Br_6 \leftrightharpoons 2AlBr_3$ and $Al_2Cl_6 \leftrightharpoons 2AlCl_3$, were estimated using both RGE simulations and thermodynamic calculations based on the equation of state model. For RGE calculations, critical points have been determined by fitting the coexistence data to scaling laws Eqs. (10)-(12). Optimised parameters *A, B, C* and *D* are collected in Section S5 of the Supplementary Material. For EoS based calculations, the critical point has been numerically determined as the condition where $\rho_l = \rho_v$. The resulting values are reported in Table 10 and Table 11 and are systematically compared with the experimental values available in the literature and presented in Table 8 and Table 9. Critical-point estimates based on Eqs. (10)-(12) were also obtained by treating β as a free fitting parameter. The resulting deviations remain below 1 % for T_c and ρ_c, and below 5 % for P_c. This limited sensitivity is consistent with the weak reactivity exhibited by the systems investigated in this study. The corresponding fitted values are reported in Table S16 of the Supplementary Material.

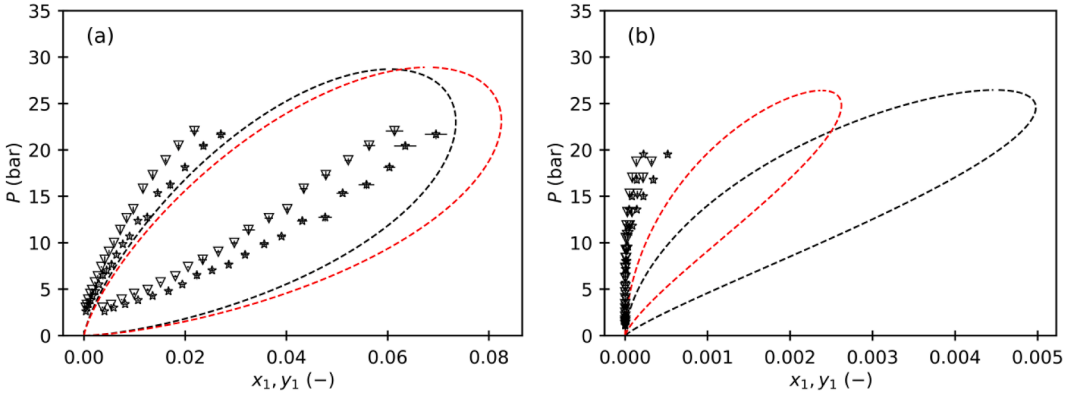

Fig. 7. Pressure-monomer composition ($P - \{x_1, y_1\}$) diagrams for the reactive mixtures: (a) $Al_2Br_6 \leftrightharpoons 2AlBr_3$ and (b) $Al_2Cl_6 \leftrightharpoons 2AlCl_3$. The mole fraction x_1 refers to the molar composition of the monomer (AlX_3) in the liquid phase, while y_1 denotes its composition in the vapor phase. The black dotted curve represents the reference curve obtained by equation of state modelling using JANAF thermochemical data (Table 3), while the red dotted curves represent results obtained using QM data computed in this work (Table 2). Black downward triangles represent RGE simulation results obtained with Lennard-Jones parameters fitted to (T_c, V_c) values; black stars represent RGE simulation results using (T_c, P_c) values. RGE simulation results include error bars, which are smaller than the symbols and thus not visible.

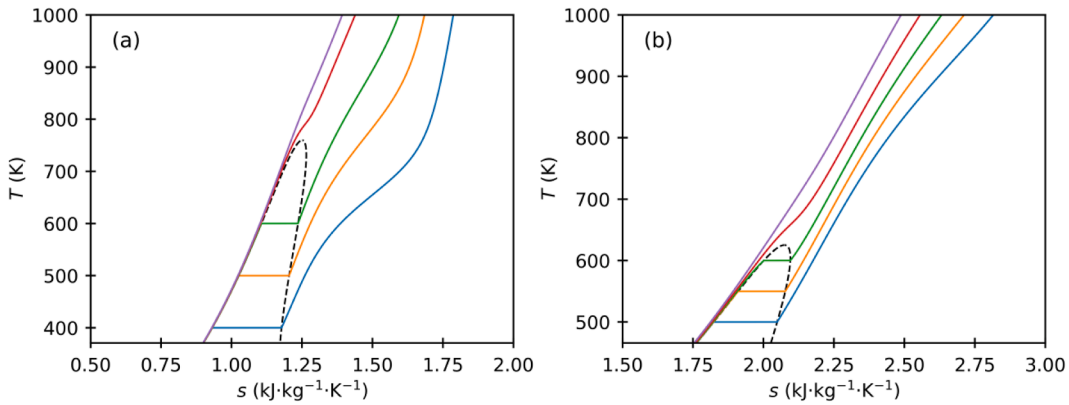

Fig. 8. Temperature-entropy ($T-s$) diagram with isobars for the reactive mixtures: (a) $Al_2Br_6 \leftrightharpoons 2AlBr_3$ and (b) $Al_2Cl_6 \leftrightharpoons 2AlCl_3$, computed by equation of state modelling. The black dotted curve represents the reference curve obtained using JANAF thermochemical data [32] (*Table 3*). Coloured solid lines correspond to isobars computed at different pressures: blue curve at the saturation pressure of the fluid at: (a) 400 K and (b) 500 K; orange at the VLE pressure of the fluid at: (a) 500 K and (b) 550 K; green at the VLE pressure of the fluid at 600 K; red at 40 bar; and purple at 80 bar. The minimum temperature of the plots is fixed to the triple point temperature of the relative fluid.

Table 8
Literature critical points of $Al_2Cl_6 \leftrightharpoons 2AlCl_3$ at chemical equilibrium.

Reference	T_c (K)	P_c (bar)	ρ_c (kg·m^{-3})
[69]	620 ± 2	-	510.6
[55,70]	625.65 ± 0.5	26.5 ± 0.1	510
[57]	627.15	-	505
[71]	629.5	-	-

Table 9
Literature critical points of $Al_2Br_6 \leftrightharpoons 2AlBr_3$ at chemical equilibrium.

Reference	T_c (K)	P_c (bar)	ρ_c (kg·m^{-3})
[53]	763 ± 2	-	860.5 ± 2.3
[54]	767.15	-	860
[61]	-	28.88 ± 0.61	-
[71]	772	-	-
[72]	768.15	27.05	887.5

The reference experimental critical point of the reactive fluid $Al_2Cl_6 \leftrightharpoons 2AlCl_3$ has been determined from the arithmetic mean of literature data compiled in Table 8, yielding a critical temperature of $T_c = 626$ K, a critical pressure of $P_c = 26.5$ bar, and a critical density of $\rho_c = 509$ kg·m^{-3}. For the reactive mixture $Al_2Br_6 \leftrightharpoons 2AlBr_3$, the literature values reported in Table 9 provide the mean critical parameters $T_c = 768$ K, $P_c = 28.0$ bar, and $\rho_c = 869$ kg·m^{-3}.

For the $Al_2Cl_6 \leftrightharpoons 2AlCl_3$ system, the relative deviations between RGE simulation results (Table 10) and experimental data are 0.6 % for critical temperature, considering both (T_c, P_c) and (T_c, V_c)-parameter set, 13.6 % and 0.3 % for P_c and ρ_c, respectively, with (T_c, P_c) set and 1.9 % and 11.0 % for P_c and ρ_c, respectively, with (T_c, V_c) set. For the $Al_2Br_6 \leftrightharpoons 2AlBr_3$ system, the critical temperatures predicted in this work by both sets of Monte Carlo simulations show satisfactory agreement with the mean literature values, with a MAPE of about 1.4 % in both cases (Table 10). Specifically, for the (T_c, P_c)-based potential, the MAPEs are 7.7 % in pressure and 14.6 %

Table 10
Critical point estimations from RGE calculations using Eqs. (10)–(12). Uncertainties are calculated using the error propagation law on the basis of the uncertainties of RGE calculations.

Input data pair used for σ - parameter calculation	Reaction	T_c (K)	P_c (bar)	ρ_c (kg·m^{-3})
(T_c, V_c)	$Al_2Cl_6 \leftrightharpoons 2AlCl_3$	622.1 ± 0.3	30.1 ± 0.2	507.7 ± 0.6
	$Al_2Br_6 \leftrightharpoons 2AlBr_3$	757.7 ± 0.5	34.3 ± 0.2	885 ± 1
(T_c, P_c)	$Al_2Cl_6 \leftrightharpoons 2AlCl_3$	622.3 ± 0.3	27.0 ± 0.2	453.1 ± 0.6
	$Al_2Br_6 \leftrightharpoons 2AlBr_3$	757.8 ± 0.5	30.3 ± 0.2	758 ± 1

Table 11
Critical point estimations from EoS calculations at chemical equilibrium.

Input ideal gas properties	Reaction	T_c (K)	P_c (bar)	ρ_c (kg·m^{-3})
JANAF	$Al_2Cl_6 \leftrightharpoons 2AlCl_3$	625.32	26.46	439.47
	$Al_2Br_6 \leftrightharpoons 2AlBr_3$	759.69	28.70	740.19
QM	$Al_2Cl_6 \leftrightharpoons 2AlCl_3$	625.50	26.41	439.37
	$Al_2Br_6 \leftrightharpoons 2AlBr_3$	758.62	28.90	740.88

Table 12
Critical pressure estimation from RGE calculations, using Eq. (19). A, B and C parameters are reported in the Supplementary Material (Table S17). Uncertainties are calculated using the error propagation law on the basis of the uncertainties of RGE calculations.

Input data pair used for σ - parameter calculation	Reaction	P_c (bar)
(T_c, V_c)	$Al_2Cl_6 \leftrightharpoons 2AlCl_3$	33.0 ± 0.1
	$Al_2Br_6 \leftrightharpoons 2AlBr_3$	36.9 ± 0.1
(T_c, P_c)	$Al_2Cl_6 \leftrightharpoons 2AlCl_3$	30.9 ± 0.1
	$Al_2Br_6 \leftrightharpoons 2AlBr_3$	34.1 ± 0.1

in density. In contrast, the (T_c, V_c)-based potential results in a larger deviation for pressure (18.5 %) but significantly smaller for density (1.8 %). As observed in Section 3.2.2, the accuracy of the calculated properties (pressures or densities) reflects the properties chosen to define the set of parameters, (T_c, P_c) or (T_c, V_c), respectively.

Moreover, equation of state-based estimations using ideal gas thermodynamic data from the JANAF tables (Table 3) result in MAPEs of 1.1 % for T_c, 2.5 % for P_c, and 17.4 % for ρ_c. When replacing the JANAF input with ab-initio quantum data calculated at the CBS-QB3 level of theory (Table 2), deviations shift to 2.4 % for T_c, 8.2 % for P_c, and 16.6 % for ρ_c. These results demonstrate the ability of quantum chemistry-based thermodynamic data to serve as a robust alternative in the absence of reliable experimental databases.

Additionally, as an alternative to using Eq. (12), critical pressures were also obtained by fitting MC results and using the pressure at VLE given by Antoine correlation, Eq. (19). The resulting critical pressures are reported in Table 12 and the fitted correlations are provided in Table S17 of the Supplementary Material.

$$\ln P^{VLE} = A - \frac{B}{C+T} \tag{19}$$

Despite offering a more precise fit to the MC data, this more complex correlation produces larger deviations from the experimental critical-point values than those reported in Tables 8 and 9.

For completeness, the methodology applied in this work to $Al_2Cl_6 \leftrightharpoons 2AlCl_3$ and $Al_2Br_6 \leftrightharpoons 2AlBr_3$ has also been applied to the system $N_2O_4 \leftrightharpoons 2NO_2$, for which the mean experimental critical parameters are reported as $T_c = 431.3$ K, $P_c = 101.3$ bar, and $\rho_c = 558.4$ kg·m^{-3} [11]. By considering critical properties of the monomer and dimer species calculated by Lasala et al. [10], the single-site Lennard-Jones parameter sets (T_c, V_c) have been firstly derived from Eqs. (7) and (9):

$$\sigma_{NO_2} = 3.685 \text{ Å}, \ \epsilon_{NO_2}/k_B = 216.743 \ K$$

$$\sigma_{N_2O_4} = 4.546 \text{ Å}, \ \epsilon_{N_2O_4}/k_B = 371.889 \ K$$

Then, RGE simulations have been performed on the reactive system $N_2O_4 \leftrightharpoons 2NO_2$ and its critical point parameters have been derived from Eqs. (10)-(12), giving: $T_c = 428 \pm 1$ K, $P_c = 100 \pm 1$ bar and $\rho_c = 543 \pm 1$ kg·m^{-3}. The application of this methodology results in MAPEs for T_c, P_c and ρ_c equal to 0.8 %, 1.3 % and 2.8 %, with respect to mean experimental data. The accuracy of these results is satisfactory and supports the use of single-site Lennard–Jones potentials for predicting first-order approximation vapour-liquid equilibrium properties of dimerising systems.

4. Conclusions

This work presents a methodology for modelling the phase equilibrium properties of dimerising fluids, which requires, as input, only the critical point properties and acentric factors of the species forming the reactive mixture. This approach is based on ab-initio quantum mechanical calculations to determine the molecular ideal gas properties, including standard enthalpy ($\Delta_f H^\circ$), entropy (S°), and heat capacity (C_p). These properties are then used to evaluate real fluid thermodynamics through both an equation of state and molecular Monte Carlo simulations.

The equation of state employed in this work is the cubic Peng-Robinson model, coupled with the a-thermal version of EoS/$a_{res}^{E,\gamma}$ mixing rules. This model is entirely predictive, as it does not require any binary interaction parameters. Monte Carlo simulations are performed by modelling molecules as single particles interacting via the Lennard-Jones potential. This simplified representation allows for the derivation of Lennard-Jones (σ, ϵ)-parameters based on the known critical-point properties of the molecules. More specifically, (σ, ϵ)-parameters have been derived either from (T_c, V_c), or from (T_c, P_c) and the results have been compared.

Two systems were evaluated to assess the accuracy of the overall approach: $Al_2Br_6 \leftrightharpoons 2AlBr_3$ and $Al_2Cl_6 \leftrightharpoons 2AlCl_3$. For these systems, the critical properties (T_c, P_c, V_c) of both the monomers and dimers were found in the literature. However, such data are typically unavailable for many species that undergo dimerization. In these cases, machine learning models or group contribution methods could offer valuable alternatives for predicting the necessary critical properties.

When compared to the available experimental data of $Al_2Br_6 \leftrightharpoons 2AlBr_3$ and $Al_2Cl_6 \leftrightharpoons 2AlCl_3$, the equation of state provides significantly more accurate results than Monte Carlo (MC) simulations, likely due to the simplified single-particle LJ potential used in MC simulations. Further comparison of the MC simulations revealed that the (σ, ϵ)-parameters derived from available critical temperature (T_c) and volume (V_c) data yield more precise volumetric properties than those obtained from critical temperature and pressure (P_c) data. However, while the MC simulations provided acceptably accurate volumetric properties, the accuracy of the VLE pressures remains limited.

Moreover, both the EoS and MC modelling revealed that the systems exhibit only weak reactivity under saturated vapor or liquid conditions, with the extent of reactivity increasing significantly at higher temperatures.

Building on previous studies applied to the dissociating N_2O_4 system [10,11], this work demonstrates the reliability of the employed equation of state model and thus its applicability to novel reactive systems for determining first-order approximation vapour-liquid equilibrium properties. However, the accuracy of MC simulations remains limited due to the use of a simplified single-particle intermolecular potential. To enhance these simulations, the next step will be to develop a more refined potential that accounts for molecular polarizability.

CRediT authorship contribution statement

Julien Joliat: Writing – original draft, Visualization, Validation, Software, Investigation, Formal analysis, Data curation, Conceptualization. **Konstantin Samukov:** Software, Investigation. **Rachid Hadjadj:** Writing – original draft, Investigation. **Thijs J.H. Vlugt:** Writing – review & editing, Supervision, Methodology. **Olivier Herbinet:** Writing – review & editing, Investigation. **Silvia Lasala:** Writing – review & editing, Writing – original draft, Validation, Supervision, Project administration, Methodology, Investigation, Funding acquisition, Formal analysis, Conceptualization.

Declaration of competing interest

The authors declare that they have no known competing financial interests or personal relationships that could have appeared to influence the work reported in this paper.

Acknowledgements

This work has received funding from the European Research Council (ERC) under the European Union's Horizon Europe research and innovation program (grant agreement No. 101040994). High Performance Computing resources were partially provided by the EXPLOR centre hosted by the Université de Lorraine.

Supplementary materials

Supplementary material associated with this article can be found, in the online version, at doi:10.1016/j.fluid.2026.114661.

Data availability

Data will be made available on request.

References

[1] M.J. Moran, H.N. Shapiro, D.D. Boettner, Fundamentals of Engineering Thermodynamics,, 7th Edition, Wiley Global Education, 2010.
[2] Energy IEA, Technol. Perspect. (2023) 2023.
[3] M. Astolfi, D. Alfani, S. Lasala, E. Macchi, Comparison between ORC and CO2 power systems for the exploitation of low-medium temperature heat sources, Energy 161 (2018) 1250–1261, https://doi.org/10.1016/j.energy.2018.07.099.
[4] E. Macchi, 1 – Theoretical basis of the organic rankine cycle, Org. Rank. Cycle (ORC) Power Syst. (2017) 3–24, https://doi.org/10.1016/B978-0-08-100510-1.00001-6.
[5] European Commission, Reactive fluids for intensified thermal energy conversion - REACHER, CORDIS (2022). https://cordis.europa.eu/project/id/101040994/results.
[6] European Commission, Carboxylic acids as REAcTIVE refrigerants to make heat pumps efficient - CREATIVE, CORDIS (2025). https://cordis.europa.eu/project/id/101213389.
[7] S. Lasala, R. Privat, O. Herbinet, P. Arpentinier, D. Bonalumi, J.-N. Jaubert, Thermo-chemical engines: unexploited high-potential energy converters, Energy Convers. Manag. 229 (2021) 113685, https://doi.org/10.1016/j.enconman.2020.113685.
[8] S. Lasala, Towards an improved thermodynamic modelling and enhanced efficiency of energy conversion systems, accreditation to supervise research, Université de Lorraine, 2024. https://hal.univ-lorraine.fr/tel-04513361.
[9] A. Barakat, S. Lasala, P. Arpentinier, J.-N. Jaubert, The original and impactful exploitation of chemical energy in heat pumps, Chem. Eng. J. Adv. 12 (2022) 100400, https://doi.org/10.1016/j.ceja.2022.100400.
[10] S. Lasala, K. Samukov, H. Mert Polat, V. Lachet, O. Herbinet, R. Privat, J.-N. Jaubert, O.A. Moultos, K. De Ras, T.J.H. Vlugt, Application of thermodynamics at different scales to describe the behaviour of fast reacting binary mixtures in

vapour-liquid equilibrium, Chem. Eng. J. 483 (2024) 148961, https://doi.org/10.1016/j.cej.2024.148961.
[11] K. Samukov, D. Vega-Maza, E.W. Lemmon, V. Diky, S. Lasala, An accurate thermodynamic model to characterise dissociating N2O4 at vapour–Liquid equilibrium states, Int. J. Thermophys. 46 (2025) 95, https://doi.org/10.1007/s10765-025-03565-x.
[12] S. Lasala, P. Chiesa, R. Privat, J.-N. Jaubert, VLE properties of CO2 – Based binary systems containing N2, O2 and Ar: experimental measurements and modelling results with advanced cubic equations of state, Fluid Ph. Equilib. 428 (2016) 18–31, https://doi.org/10.1016/j.fluid.2016.05.015.
[13] H.M. Polat, S. Lasala, F. De Meyer, Scaling towards the critical point in the combined reaction/Gibbs ensemble, Fluid. Ph. Equilib. 582 (2024) 114084, https://doi.org/10.1016/j.fluid.2024.114084.
[14] R. Bounaceur, F. Paes, R. Privat, J.-N. Jaubert, AI-powered prediction of critical properties and boiling points: a hybrid ensemble learning and QSPR approach, J. Cheminform. 17 (2025) 132, https://doi.org/10.1186/s13321-025-01062-9.
[15] D. Frenkel, B. Smit, Understanding molecular simulation: from algorithms to applications, 3rd edition, Elsevier, 2023.
[16] M.P. Allen, D.J. Tildesley, Computer simulation of liquids, 2nd edition, Oxford University Press, 2017.
[17] M.J. Frisch, G.W. Trucks, H.B. Schlegel, G.E. Scuseria, M.A. Robb, J.R. Cheeseman, G. Scalmani, V. Barone, B. Mennucci, G.A. Petersson, H. Nakatsuji, M. Caricato, X. Li, H.P. Hratchian, A.F. Izmaylov, J. Bloino, G. Zheng, J.L. Sonnenberg, M. Hada, M. Ehara, K. Toyota, R. Fukuda, J. Hasegawa, M. Ishida, T. Nakajima, Y. Honda, O. Kitao, H. Nakai, T. Vreven, J.A. Montgomery, J.E. Peralta, F. Ogliaro, M. Bearpark, J.J. Heyd, E. Brothers, K.N. Kudin, V.N. Staroverov, R. Kobayashi, J. Normand, K. Raghavachari, A. Rendell, J.C. Burant, S.S. Iyengar, J. Tomasi, M. Cossi, N. Rega, J. M. Millam, M. Klene, J.E. Knox, J.B. Cross, V. Bakken, C. Adamo, J. Jaramillo, R. Gomperts, R.E. Stratmann, O. Yazyev, A.J. Austin, R. Cammi, C. Pomelli, J.W. Ochterski, R.L. Martin, K. Morokuma, V.G. Zakrzewski, G.A. Voth, P. Salvador, J.J. Dannenberg, S. Dapprich, A.D. Daniels, Ö. Farkas, J.B. Foresman, J.V. Ortiz, J. Cioslowski, D.J. Fox, Gaussian 09 revision B.01, (2010).
[18] J.A. Montgomery Jr, M.J. Frisch, J.W. Ochterski, G.A. Petersson, A complete basis set model chemistry. VII. use of the minimum population localization method, J. Chem. Phys. 112 (2000) 6532–6542, https://doi.org/10.1063/1.481224.
[19] J.A. Montgomery Jr., M.J. Frisch, J.W. Ochterski, G.A. Petersson, A complete basis set model chemistry. VII. Use of the minimum population localization method, J. Chem. Phys. 112 (2000) 6532–6542, https://doi.org/10.1063/1.481224.
[20] J.A. Montgomery Jr., M.J. Frisch, J.W. Ochterski, G.A. Petersson, A complete basis set model chemistry. VI. Use of density functional geometries and frequencies, J. Chem. Phys. 110 (1999) 2822–2827.
[21] J.M. Simmie, K.P. Somers, Benchmarking compound methods (CBS-QB3, CBS-APNO, G3, G4, W1BD) against the active thermochemical tables: a litmus test for cost-effective molecular formation enthalpies, J. Phys. Chem. A 119 (2015) 7235–7246, https://doi.org/10.1021/jp511403a.
[22] C.A.R. Pappijn, F.H. Vermeire, R. Van de Vijver, M.-F. Reyniers, G.B. Marin, K. M. Van Geem, Bond additivity corrections for CBS-QB3 calculated standard enthalpies of formation of H, C, O, N, and S containing species, Int. J. Chem. Kinet. 53 (2021) 345–355, https://doi.org/10.1002/kin.21447.
[23] N. Vin, F. Battin-Leclerc, O. Herbinet, A study of thermal decomposition of bromoethane, J. Anal. Appl. Pyrolysis 136 (2018) 199–207, https://doi.org/10.1016/j.jaap.2018.10.005.
[24] L.A. Curtiss, K. Raghavachari, P.C. Redfern, J.A. Pople, Assessment of gaussian-2 and density functional theories for the computation of enthalpies of formation, J. Chem. Phys. 106 (1997) 1063–1079, https://doi.org/10.1063/1.473182.
[25] A. Nicolaides, A. Rauk, M.N. Glukhovtsev, L. Radom, Heats of formation from G2, G2 (MP2), and G2 (MP2, SVP) total energies, J. Phys. Chem. 100 (1996) 17460–17464, https://doi.org/10.1021/jp9613753.
[26] C.J. Cramer, Essentials of computational chemistry: theories and models, 2nd ed., John Wiley & Sons, Chichester; Hoboken, NJ; San Francisco, 2004.
[27] V. Van Speybroeck, R. Gani, R.J. Meier, The calculation of thermodynamic properties of molecules, Chem. Soc. Rev. 39 (2010) 1764–1779, https://doi.org/10.1039/B809850F.
[28] Russell D. Johnson I.I.I. (ed.), NIST Computational Chemistry Comparison and Benchmark Database, (2022). https://doi.org/10.18434/T47C7Z.
[29] J.D. Cox, D.D. Wagman, V.A. Medvedev, CODATA key values for thermodynamics, (1989). https://doi.org/10.1002/bbpc.19900940121.
[30] A. Miyoshi, GPOP Softw. (2022). http://akrmys.com/gpop/.
[31] F.A. Aly, L.L. Lee, Self-consistent equations for calculating the ideal gas heat capacity, enthalpy, and entropy, Fluid Ph. Equilib. 6 (1981) 169–179, https://doi.org/10.1016/0378-3812(81)85002-9.
[32] M.W. Chase, NIST-JANAF Thermochemical Tables 4th ed, J. Phys. Chem. Reffernce Data. (1998) 1529–1564, https://doi.org/10.18434/T42S31.
[33] P. Schwerdtfeger, D.J. Wales, 100 years of the Lennard-Jones potential, J. Chem. Theory Comput. 20 (2024) 3379–3405, https://doi.org/10.1021/acs.jctc.4c00135.
[34] S. Stephan, M. Thol, J. Vrabec, H. Hasse, Thermophysical properties of the Lennard-Jones Fluid: database and data assessment, J. Chem. Inf. Model 59 (2019) 4248–4265, https://doi.org/10.1021/acs.jcim.9b00620.
[35] A.M. Borovikova, A.V. Zinov'ev, B.G. Maksimov, A.A. Moliboško, Viscosity of dissociating aluminium halides in dense gas state, Vescì Akad. Navuk BSSR. Seryâ Fiz.-Energ. Navuk (1970) 85–89.
[36] A.Z. Panagiotopoulos, Direct determination of phase coexistence properties of fluids by Monte Carlo simulation in a new ensemble, Mol. Phys. 61 (1987) 813–826, https://doi.org/10.1080/00268978700101491.
[37] A.Z. Panagiotopoulos, N. Quirke, M. Stapleton, D.J. Tildesley, Phase equilibria by simulation in the Gibbs ensemble: alternative derivation, generalization and application to mixture and membrane equilibria, Mol. Phys. 63 (1988) 527–545, https://doi.org/10.1080/00268978800100361.
[38] R. Hens, A. Rahbari, S. Caro-Ortiz, N. Dawass, M. Erdős, A. Poursaeidesfahani, H. S. Salehi, A.T. Celebi, M. Ramdin, O.A. Moultos, D. Dubbeldam, T.J.H. Vlugt, Brick-CFCMC: open source software for Monte Carlo simulations of phase and reaction equilibria using the continuous fractional component method, J. Chem. Inf. Model. 60 (2020) 2678–2682, https://doi.org/10.1021/acs.jcim.0c00334.
[39] A. Rahbari, R. Hens, M. Ramdin, O.A. Moultos, D. Dubbeldam, T.J.H. Vlugt, Recent advances in the continuous fractional component Monte Carlo methodology, Mol. Simul. 47 (2021) 804–823, https://doi.org/10.1080/08927022.2020.1828585.
[40] H.M. Polat, H.S. Salehi, R. Hens, D.O. Wasik, A. Rahbari, F. De Meyer, C. Houriez, C. Coquelet, S. Calero, D. Dubbeldam, O.A. Moultos, T.J.H. Vlugt, New features of the open source Monte Carlo software brick-CFCMC: thermodynamic integration and hybrid trial moves, J. Chem. Inf. Model 61 (2021) 3752–3757, https://doi.org/10.1021/acs.jcim.1c00652.
[41] A.D. Cortés Morales, I.G. Economou, C.J. Peters, J. Ilja Siepmann, Influence of simulation protocols on the efficiency of Gibbs ensemble Monte Carlo simulations, Mol. Simul. 39 (2013) 1135–1142, https://doi.org/10.1080/08927022.2013.828209.
[42] P. Ungerer, B. Tavitian, A. Boutin, Applications of molecular simulation in the oil and gas industry: monte Carlo methods, Editions Technip, 2005.
[43] J.K. Johnson, A.Z. Panagiotopoulos, K.E. Gubbins, Reactive canonical Monte Carlo: a new simulation technique for reacting or associating fluids, Mol. Phys. 81 (1994) 717–733, https://doi.org/10.1080/00268979400100481.
[44] W. Smith, B. Triska, The reaction ensemble method for the computer simulation of chemical and phase equilibria. I. Theory and basic examples, J. Chem. Phys. 100 (1994) 3019–3027, https://doi.org/10.1063/1.466443.
[45] C.Heath Turner, J.K. Brennan, M. Lísal, W.R. Smith, J. Karl Johnson, K.E. Gubbins, Simulation of chemical reaction equilibria by the reaction ensemble Monte Carlo method: a review, Mol. Simul. 34 (2008) 119–146, https://doi.org/10.1080/08927020801986564.
[46] A. Poursaeidesfahani, R. Hens, A. Rahbari, M. Ramdin, D. Dubbeldam, T.J. H. Vlugt, Efficient application of continuous fractional component monte Carlo in the reaction ensemble, J. Chem. Theory Comput. 13 (2017) 4452–4466.
[47] T.H.G. Saji, T.J.H. Vlugt, S. Calero, B. Bagheri, Modeling nitric oxide and its dimer: force field development and thermodynamics of dimerization, Phys. Chem. Chem. Phys. 27 (2025) 13662–13674, https://doi.org/10.1039/D5CP00784D.
[48] D.-Y. Peng, D.B. Robinson, A new two-constant equation of State, Ind. Eng. Chem. Fundam. 15 (1976) 59–64, https://doi.org/10.1021/i160057a011.
[49] J.R. Elliott, C.T. Lira, Introductory chemical engineering thermodynamics, Introductory chemical engineering thermodynamics, 2012.
[50] W. Biltz, A. Voigt, Über den leitfähigkeitsabfall schmelzenden aluminiumchlorids und die konstitution der aluminiumhalogenide, Z. Anorg. Allg. Chem. 126 (1923) 39–53, https://doi.org/10.1002/zaac.19231260103.
[51] E.A. Gorenbejn, Physico-chemical investigation of the systems SbBr3 - AlBr3, ZnBr2 - AlBr3 and KBr - AlBr3 in the molten state (viscosity, electroconducitivty and specific weight isotherms), Ž. Obŝ. Khimii. 15 (1945) 729–744.
[52] M.A. Kločko, Investigation of non-aqueous solutions by methods of physico-chemical analysis. II. Electro-conductivity, viscosity and specific gravity of the binary system AlBr3 - C6H5NO2, Izvestiâ Akademii Nauk SSSR, Otd. Mat. Estestv. Nauk (1937) 647–673.
[53] J.W. Johnson, W.J. Silva, D. Cubicciotti, Critical temperature and coexistence curve for aluminum bromide, J. Phys. Chem. 72 (1968) 1664–1668, https://doi.org/10.1021/j100851a048.
[54] L.A. Nisel'son, T.D. Sokolova, R.K. Nikolaev, Orthobaric densities and critical parameters of a number of higher bromides and iodides of elements of groups III and IV of the periodic table, Teplofiz. Svojstva Veshchestv Mater. 2 (1970) 246–255.
[55] N.D. Denisova, A.P. Baskova, Saturated vapour pressure and critical parameters of aluminum chloride, Ž. Fiz. Khimii 43 (1969) 2353–2354.
[56] J.W. Johnson, D. Cubicciotti, W.J. Silva, The critical temperature, orthobaric densities, and volume change on fusion for aluminum chloride, High Temp. Sci. 3 (1971) 523–532.
[57] L.A. Nisel'son, T.D. Sokolova, Density, viscosity and surface tension of aluminum and gallium trichlorides, Ž. Neorg. Khimii 10 (1965) 1216–1519.
[58] L.A. King, D.W. Seegmiller, Liquid and vapor densities of aluminum chloride, J. Chem. Eng. Data. 16 (1971) 23–26, https://doi.org/10.1021/je60048a008.
[59] Y. Sato, Y. Matsuzaki, M. Uda, Y. Sasaki, T. Nohira, Density, viscosity and surface tension of molten aluminum chloride, Electrochemistry 67 (1999) 568–572, https://doi.org/10.5796/electrochemistry.67.568.
[60] W. Fischer, O. Rahlfs, B. Benze, Dampfdrucke und dampfdichten von Aluminiumhalogeniden, Z. Anorg. Allg. Chem. 205 (1932) 1–41, https://doi.org/10.1002/zaac.19322050102.
[61] J.W. Johnson, W.J. Silva, D. Cubicciotti, The vapor pressure and enthalpy of vaporization of molten aluminum bromide to the critical point, J. Phys. Chem. 72 (1968) 1669–1672, https://doi.org/10.1021/j100851a049.
[62] L.A. Nisel'son, A.I. Pustil'nik, O.P. Gavrilov, V.A. Rodin, Liquid-solid and Liquid-vapour equilibrium in the NbCl5-Al2Cl6 system, Ž. Neorg. Khimii. 10 (1965) 2339–2346.
[63] V.A. Smits, J.L. Meyering, M.A. Kamermans, Die komplexität des aluminiumchlorids, I Proc. KNAW 34 (1931) 1327–1339.
[64] V.A. Smits, J.L. Meyering, M.A. Kamermans, Die komplexität des aluminiumchlorids, II Proc. KNAW 35 (1932) 193–196.
[65] A. Smits, J.L. Meijering, Die komplexität des aluminiumchlorids, Z. Phys. Chem. 41 (1938) 98–111, https://doi.org/10.1515/zpch-1938-4110.

[66] W.D. Treadwell, L. Terebesi, Zur kenntnis der Chlorierung von Aluminiumoxyd mit chlor und kohle, Helv. Chim. Acta. 15 (1932) 1053–1066, https://doi.org/10.1002/hlca.193201501115.
[67] J.T. Viola, D.W. Seegmiller, A.A.Jr. Fannin, L.A. King, Vapor pressure of aluminum chloride systems. 1. Vapor pressure and triple point of pure aluminum chloride, J. Chem. Eng. Data. 22 (1977) 367–370, https://doi.org/10.1021/je60075a003.
[68] S. Lasala, R. Privat, J.-N. Jaubert, Inert and reactive working fluids for closed power cycles: present knowledge, applications and open researches, organic rankine cycle technology for heat recovery (2018). https://doi.org/10.5772/intechopen.79290.
[69] J.W. Johnson, D. Cubicciotti, W.J. Silva, The critical temperature, orthobaric densities, and volume change on fusion for aluminum chloride, High Temp. Sci. 3 (1971) 523–532.
[70] N.D. Denisova, Fazovye ravnovesiya v odnokomponentnykh i dvukhkomponentnykh Sistemakh, obrazovannykh tetrachloridami tsirkoniya I Gafniya I khloristym alyuminiem, abstract of PhD thesis in chemical sciences, State research and design institute of rare metals and industrial technologies "GIREDMET, 1966.
[71] L. Rotinjanz, W. Suchodski, Bestimmung der kritischen temperatur der aluminium- und antimonhalogenide, Z. Phys. Chem. 87 (1914) 635–637, https://doi.org/10.1515/zpch-1914-8744.
[72] D.I. Žuravlev, Heat of vaporization, orthobaric densities and critical data of aluminum bromide, Ž. Fiz. Him. 10 (1937) 325–329.